Cortical waves mediate the cellular response to electric fields

Authors: Qixin Yang[1,2], Yuchuan Miao[3], Leonard J. Campanello[1,2], Matt J. Hourwitz[4], Bedri Abubaker-Sharif[3], Abby L. Bull[1,2], Peter N. Devreotes[3], John T. Fourkas[2,4], Wolfgang Losert[1,2]*.

Affiliations:

[1]Department of Physics, University of Maryland, College Park, MD 20742

[2]Institute for Physical Science and Technology, University of Maryland, College Park, MD 20742

[3]Department of Cell Biology, Johns Hopkins University, Baltimore, MD 21218

[4]Department of Chemistry & Biochemistry, University of Maryland, College Park, MD 20742

*Correspondence to: wlosert@umd.edu

Abstract:

Electrotaxis, the directional migration of cells in a constant electric field, is important in regeneration, development, and wound healing. Electrotaxis has a slower response and a smaller dynamic range than guidance by other cues, suggesting that the mechanism of electrotaxis share both similarities and differences with chemical-gradient-sensing pathways. We examined a mechanism centered on the excitable system consisting of cortical waves of biochemical signals coupled to cytoskeletal reorganization, which has been implicated in random cell motility. We use electro-fused giant *Dictyostelium discoideum* cells to decouple waves from cell motion and employ nanotopographic surfaces to limit wave dimensions and lifetimes. We demonstrate that wave propagation in these cells is guided by electric fields. The wave area and lifetime gradually increase in the first 10 minutes after an electric field is turned on, leading to more abundant and wider protrusions in the cell region nearest the cathode. The wave directions display "U-turn" behavior upon field reversal, and this switch occurs more quickly on nanotopography. Our results suggest that electric fields guide cells by controlling waves of signal transduction and cytoskeletal activity, which underlie cellular protrusions. Whereas surface receptor occupancy triggers both rapid activation and slower polarization of signaling pathways, electric fields appear to act primarily on polarization, explaining why cells respond to electric fields more slowly than to other guidance cues.

Introduction

Electrotaxis, which refers to the directed migration of cells under the guidance of an electric field (EF), is important in wound healing, development, and regeneration (Cortese et al., 2014; Lin et al., 2008; Zhao et al., 2006). EFs have been shown to cause several key signaling molecules to be

46 distributed asymmetrically across cells (Sato et al., 2009; Zhao et al., 2002, 2006), setting up cell
47 polarity. The one-order-of-magnitude range of EF strengths sensed by cells (Zhao et al., 2002) is
48 considerably smaller than the four-orders-of-magnitude concentration sensitivity in chemotaxis
49 (Harvath et al., 1991). Furthermore, whereas cells respond to chemical guidance cues on a time
50 scale of seconds and develop polarity over several minutes, the response to EFs can take up to 10
51 minutes or more after the EF is turned on (Wang et al., 2014; Zhao et al., 2006). These
52 differences raise the possibility that the rapid gradient sensing mechanisms do not serve as
53 primary mediators of EF sensing by cells. In this study, we examine whether, after turning on an
54 EF, the gradual polarization of the excitable biochemical networks that organize actin
55 polymerization comprises a slow-acting mediator of the cellular response to the EF.
56
57 Actin polymerization, coordinated with its associated signaling molecules, self-organizes into
58 microscale spatial regions that travel as waves across plasma membranes. These waves drive
59 various cell behaviors, such as migration and division (Bhattacharya et al., 2019; Bretschneider
60 et al., 2009; Flemming et al., 2020; Gerhardt et al., 2014; Gerisch, 2010). The wave system can
61 be described as a coupled signal transduction excitable network - cytoskeletal excitable network
62 (STEN-CEN) (Devreotes et al., 2017; Miao et al., 2019). STEN-CEN has the characteristics of
63 an excitable system, including exhibiting an activation threshold for wave initiation and
64 experiencing refractory periods. It has been shown that the STEN-CEN wave properties dictate
65 protrusion properties (Miao et al., 2019). Tuning the activity levels of key components in STEN-
66 CEN changes wave patterns, which leads to the transition of protrusion profiles. An
67 activator/inhibitor, reaction/diffusion system model successfully recapitulates the experimental

results (Bhattacharya et al., 2020; Bhattacharya & Iglesias, 2018). For simplicity, here we will refer to STEN-CEN waves as cortical waves.

One challenge in investigating whether cortical waves can act as the mediators of EFs is that in many of the cell types that show a strong response to EFs, the wave area is comparable to the cell area. Furthermore, waves are generated at the leading edge of the cell during directed migration (Xu et al., 2003), so that wave dynamics are tightly coupled with cell dynamics. For instance, when a cell responds to an EF reversal, waves typically remain at the cell front as the cell turns. It is not known whether the waves drive cells to turn or the cell polarity keeps the previous leading edge more active so that this edge responds first.

To distinguish between wave response and cell motion, we produced electro-fused giant *D. discoideum* (Neumann et al., 1980) with diameters up to ten times larger than that of an individual cell. Multiple simultaneous waves can be generated across the surface contact area of a giant cell (Gerhardt et al., 2014). These waves also generate actin-filled macropinosomes on the dorsal membrane (Veltman et al., 2016). The giant cells provide an excellent opportunity to study cortical wave dynamics in multiple cell regions simultaneously.

We further use nanotopography to alter the waves' spatial structures and characteristic timescales. Upon contact with nanotopography, cells produce quasi-1D wave patches. The phenomenon of guided actin polymerization by nanotopography is known as esotaxis (Driscoll et al., 2014), which has been investigated in detail (Ketchum et al., 2018; Lee et al., 2020). There are several advantages of incorporating nanotopography in our study. First, these waves persist for a shorter

time on nanotopography than on flat surfaces, enabling us to investigate whether wave systems with different characteristic timescales respond to EFs differently. Second, waves on ridged surfaces have shorter lifetimes than those on flat surfaces, and thus only propagate in local regions of giant cells. Therefore, nanotopography allows us to distinguish between local and global mediation of the EF response.

Results

Cortical waves and cell migration can be studied independently in giant cells

We imaged cells that simultaneously expressed both limE-RFP and PH_{Crac}-GFP. The former allows us to monitor filamentous actin (F-actin), which represents CEN activities. The latter enables us to monitor phosphatidylinositol-3,4,5-trisphosphate (PIP3), an indicator of STEN activities. In single, differentiated cells, usually only one wave is generated at the leading edge (Fig. 1a and Video 1), and the wave motion is coupled with cell motion. For instance, when the cell in Fig. 1a changed its direction of motion, the wave remained at the leading edge (72 s - 120 s).

In giant cells, multiple waves were initiated randomly and propagated radially across the basal membranes (Fig. 1b and Video 2). CEN is driven by STEN, but has a substantially shorter characteristic timescale. Thus, PIP3 waves displayed band-like shapes, whereas F-actin appeared across the bands with higher levels at the rims of PIP3 waves (Miao et al., 2019). As shown in Fig. 1b, colliding waves did not cross, but instead rotated by 90° (Fig. 1b, 150 s - 200 s). This behavior is suggestive of a refractory period following excitation, which is a hallmark of an excitable system. On nanoridges, the giant cells generated multiple, quasi-1D patches of F-actin

and PIP3 with shorter lifetimes than on flat surfaces (Fig. 1c and Video 3). Some waves formed and propagated for a short distance (Line 2 in Fig. 1c), whereas others formed and then quickly dissipated (Line 3 in Fig. 1c). The wave dissipation can be explained in terms of an excitable system with lateral inhibition, in which the dispersion of the inhibitor is faster than that of the activator. Thus, the waves eventually dissipate due to the spatial accumulation of the inhibitor. Prior studies have shown that in this situation, the excitable system threshold determines the wave duration (Bhattacharya et al., 2020; Ermentrout et al., 1984). As was the case on flat surfaces, 1D patches occurred throughout the basal surfaces on ridges, and thus were independent of cell motion.

Waves were also generated on the dorsal planes. In contrast to basal waves, which propagated across the surface contact (Video 2 and Video 3), dorsal waves were associated with membrane deformations, and resembled macropinosomes (Video 4). Based on 3D lattice light-sheet images of a cell plated on nanoridges (Fig. 1d and Video 5), activation of PIP3 and F-actin was correlated in both basal waves and dorsal waves. However, the dorsal waves were primarily generated in cuplike structures, whereas the stripe-like basal waves spanned the entire basal plane. In all cases, PIP3 activity was coordinated with F-actin activity (Profiles in Fig. 1a, 1b, and 1c), both in the absence (Fig. 1) and presence of an EF (Fig. 1 – figure supplement 1, Video 6). Therefore, in the experiments described below, we only monitored F-actin activity.

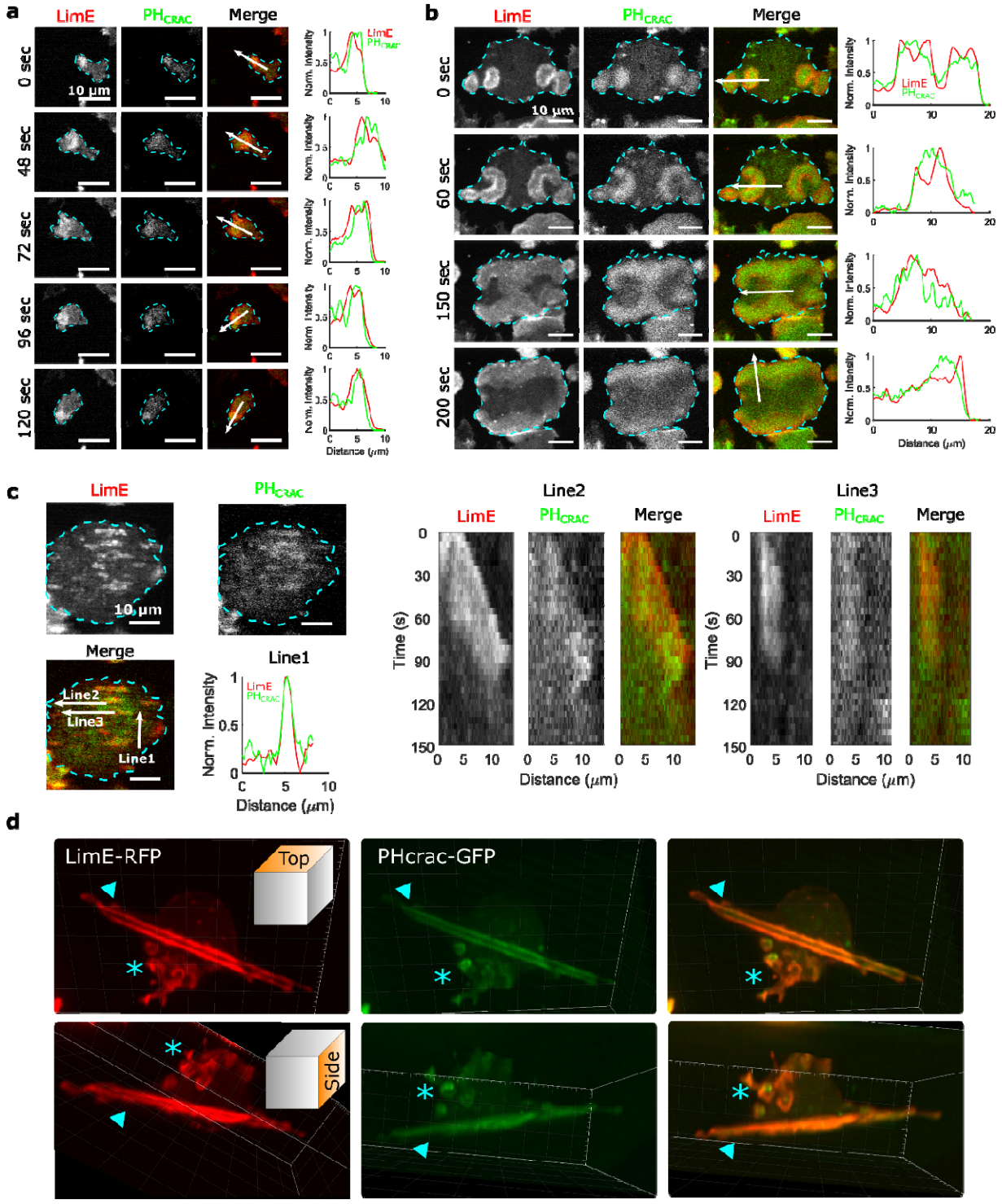

133

134 **Fig. 1. STEN-CEN waves in single cells and giant cells. a.** Snapshots of a differentiated, single

135 *D. discoideum* cell expressing limE-RFP and PHcrac-GFP, with cell boundaries denoted with

136 blue dashed lines. The right column shows the normalized intensity of limE and PHcrac from the

arrows in the merge images. The scale bars are 10 μm. **b**. Snapshots of an electrofused giant *D. discoideum* cell on a flat surface, with scanning profiles in the right column. All scale bars are 10 μm. **c.** A snapshot of an electrofused giant cell on the ridged surface. The left kymographs are from the line 2 and line 3 specified in the merged image. Line 2 shows a wave propagating along nanoridges, and line 3 shows a wave that existed briefly and then dissipated. **d.** 3D reconstruction (single time point) of a single *D. discoideum* cell plated on nanoridges, acquired using a lattice light-sheet microscope. Here we show the top aspect view (top row) and the side aspect view (bottom row). On the dorsal membrane of the cell, there are waves forming microcytotic cups (triangle) on the curved membrane, and on the basal membrane, there are streak-like waves (asterisk). The red channel represents limE-RFP, and the green channel represents PHcrac-GFP. As both the side and top views show, the dorsal waves and basal waves are independent structures, but both are composed of coordinated F-actin and PIP3.

EFs increase the area, duration, and speed of waves on nanoridges.

We found that giant cells respond to a narrow range (15 V/cm to 20 V/cm) of EF amplitudes (Video 7 and Video 8), and that higher voltage (35 V/cm) damaged cells. The 1D waves generated on nanoridges related to esotaxis enabled us to quantify the effects of a 20 V/cm EF (all EFs used here are of this magnitude, see Fig. 2 – figure supplement 1and Methods for more details about the electrotaxis experiments) on the areas, durations, and speeds of waves. Fig. 2a shows snapshots of the dynamics of F-actin in a giant cell on parallel nanoridges with a 1.6 μm spacing. In the absence of an EF (top row in Fig. 2a), individual actin polymerization events were initiated in patches on the basal surfaces (Fig. 2a and Video 9).

In the first several minutes after turning on the EF, most patches propagated as a wave along a single ridge (Fig. 2a, blue inset). After the EF was on for 10 min, some patches appeared to undergo coordinated motion across several ridges (Fig. 2a, pink inset). We calculated the ratio of F-actin occupancy to cell area, and found that an EF increased the overall level of actin polymerization by a factor of two to three (Fig. 2b). Actin patches were larger in the presence of an EF and organized into larger groups located preferentially at the cell front (bottom row in Fig. 2a, 20 min, and 25 min), leading to wider protrusions at cell fronts that drove directed cell migration (Fig. 2 – figure supplement 2). To determine whether the groups comprised a single, large wave growing across multiple ridges or multiple, small patches nucleated in close proximity, we measured the dynamics of the patches using optical flow (Lee et al., 2020), focusing on the patch edges (Fig. 2c, left image. See Methods for more details). If both edges of a patch were moving in the same direction, the structure was classified as a single, large wave. If the edges were not coordinated, the patch was classified as multiple, individual structures. This method enabled us to capture accurately waves that span across multiple ridges and are moving coordinately.

Once the large actin structures were classified, their instantaneous dimensions were measured parallel and perpendicular to the ridges (Fig. 2c). Density scatter plots of both dimensions exhibit elliptical contours (Fig. 2d), suggesting that nanotopography constrains wave growth. With an EF parallel to the ridges, the waves broadened in both directions (Fig. 2d). The average increases in wave dimension parallel and perpendicular to the ridges were 20% and 13%, respectively, and the average increase in wave area was 44%. An increase in wave duration was also observed, with the minimum wave area correlated to the duration (Fig 2e, black circles). The wave area

183 depends exponentially on the maximum wave duration (Fig. 2e, solid black lines), allowing us to
184 extract a characteristic wave time scale via
185
186 $$Area_{min} = C * e^{\frac{Duration}{T}} \quad . \qquad (1)$$
187
188 Here *C* is a constant, and *T* is the characteristic time scale, which is 48 s with no EF and 61 s in
189 the presence of a 20 V/cm EF. This difference is consistent with the EF drawing the system
190 closer to the excitability threshold. An average increase of 9% in wave propagation speed was
191 also observed in the presence of an EF (Fig. 2f).

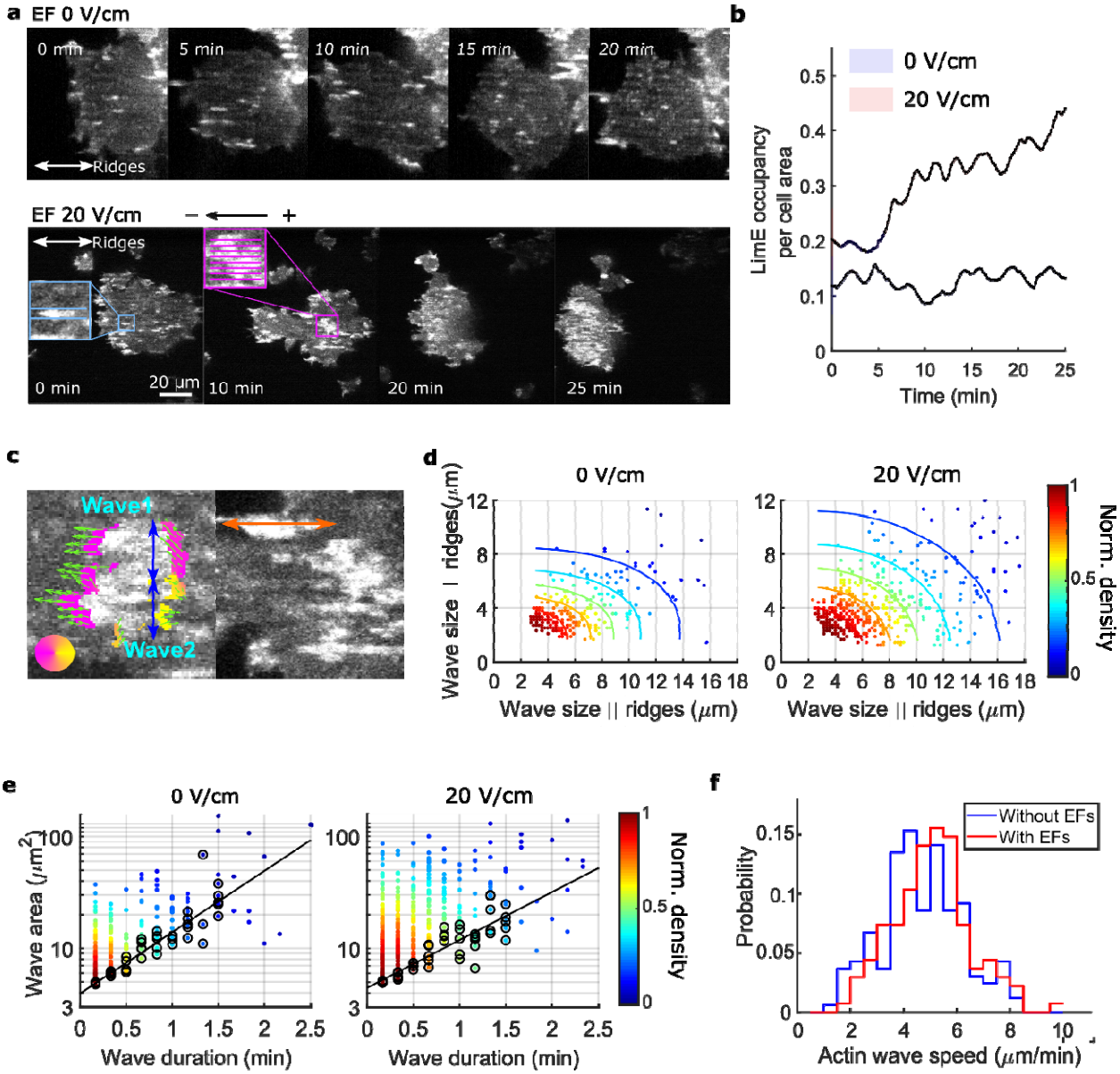

192

193 **Fig. 2. EFs alter F-actin wave properties. a.** limE images of a giant cell on nanoridges without

194 an EF (top) and in a 20 V/cm EF turned on at 0 min (bottom). **b**. The temporal change of the

195 percentage of the cell area occupied by limE without an EF (blue, N_{cell} = 5) and in a 20 V/cm EF

196 introduced at 0 min (red, N_{cell} = 4). The shaded areas represent the mean plus or minus one

197 standard deviation **c**. Division of groups of waves. The color represents the orientation of

198 optical-flow vectors according to the color wheel. The green arrows are the optical-flow vectors,

the length of which correspond to the magnitude of motion. The left image is an example of a large structure composed of two independent substructures, where the vectors at the right edge are not moving in the same direction. The wave scales in the directions perpendicular to (blue arrows) and parallel to the ridges (orange arrow) were measured on the preprocessed waves. **d.** Density scatter plots of wave scales parallel to ridges vs. perpendicular to ridges. **e.** Density scatter plots of actin-wave dimension vs. actin-wave duration. For each wave duration, the 5 points with the smallest wave areas (black circles) were selected to fit the boundaries (solid black lines). **f.** Distributions of wave propagation speeds before (blue, N_{wave} = 125) and after (red, N_{wave} = 163) applying an EF. The analyses in d-f were based on N = 4 independent experiments. The two distributions are different (Two-sample t-test, P = 0.017).

Figure 2 – source data 1. Related to Fig. 2b

Figure 2 – source data 2. Related to Fig. 2d

Figure 2 – source data 3. Related to Fig. 2e

Figure 2 – source data 4. Related to Fig. 2f

EFs guide the direction of actin waves.

Next, we consider the directional guidance of actin waves by EFs on nanoridges (Fig. 3a and Video 9) and on flat surfaces (Fig. 3b and Video 10, see Methods for details). The EF was introduced at 0 min (T_1), and in the first 2 min had little effect on the actin dynamics on any surface. On nanoridges, actin waves continued to propagate preferentially along the ridges (Fig. 3a, T_1). On flat surfaces, the waves propagated radially in groups, as seen from the broad distribution at T_1 in Fig. 3b. In the presence of an EF, the waves propagated preferentially

221 towards the cathode within ~15 min (Fig. 3a, 3b, T_2). The perpendicular spread was significantly
222 more limited on nanoridges (Fig. 3a, T_2).
223
224 The direction of the EF was reversed after the cell had commenced steady directional migration,
225 which took ~20 to 25 min. Following the field reversal, waves on ridged surfaces reoriented
226 toward the new cathode within 5 min (Fig. 3a, T_3). On flat surfaces, the wave propagation
227 direction was perpendicular to both the previous and the new EF directions at ~7 min after the
228 field reversal (Fig. 3b, T_3). Preferential propagation towards the new cathode occurred after ~13
229 min (Fig. 3b, T_4). The difference in response time between nanoridges and flat surfaces may be
230 related to the fact that waves persist longer on flat surfaces than on nanoridges (Fig. 3c).
231
232 Fig. 3d shows the continuous temporal changes of the orientation distributions. On nanoridges,
233 the preferred wave directions switched directly following EF reversal (left plot in Fig. 3d),
234 whereas on flat surfaces waves maintained a preferred direction that changed continuously in a
235 U-turn behavior (Right plot in Fig. 3d). In contrast, although single *D. discoideum* cells undergo
236 U-turns in response to EF reversal (Sato et al., 2007), giant cells did not (Video 10).
237 Wave turning may be related to differences in the patterns of wave expansion (Fig. 3e). On flat
238 surfaces, waves started from a small patch (Fig. 3e, S1) and eventually broke into band-shaped
239 waves (Fig. 3e, S4). During directed migration, the intermediate expansion of actin waves (Fig.
240 3e, S2, S3 in the top row) was biased by the EF, resulting in band-shaped waves propagating
241 preferentially towards the cathode (Fig. 3e, S4 in top row). After EF reversal, waves expanded in
242 all directions (Fig. 3e, S2, S3 in bottom row), such that optical-flow analysis captured turning
243 behavior more frequently.

244

245 We also simultaneously imaged limE-RFP at the basal plane (near the surface contact) and the
246 dorsal plane (6 µm higher). Dorsal waves (Video 11 and 12) are localized at cell fronts and
247 rearranged to the new fronts following EF reversal (Fig. 3 – figure supplement 1). Rather than
248 directly switching preferential direction, dorsal waves gradually turned toward the new cathode
249 (Fig. 3 – figure supplement 1), in a manner similar to that of basal waves on flat surfaces. Thus,
250 two different response times to EF reversal exist within the same cell, with a faster response for
251 basal waves guided by nanotopography and a slower response for the free dorsal waves. On flat
252 surfaces, the two responses are synchronized (Fig. 3 – figure supplement 2).

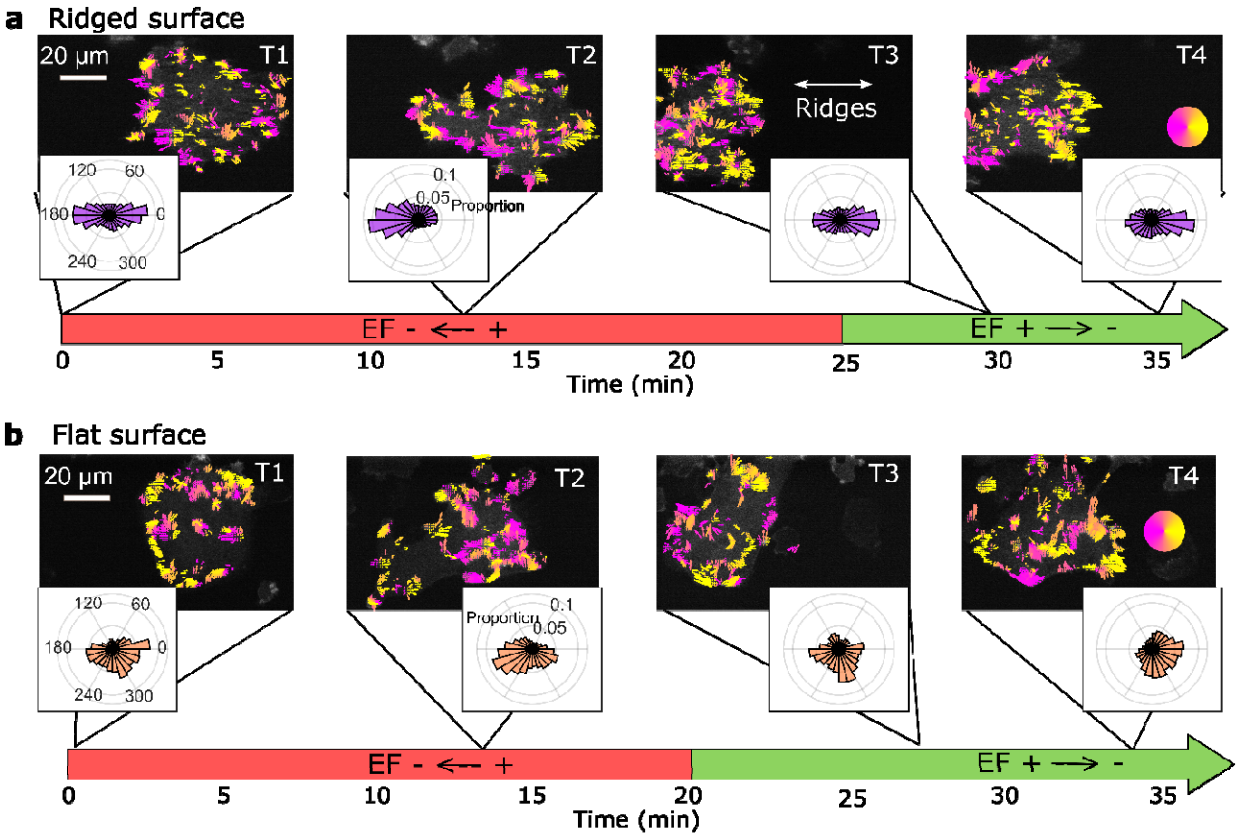

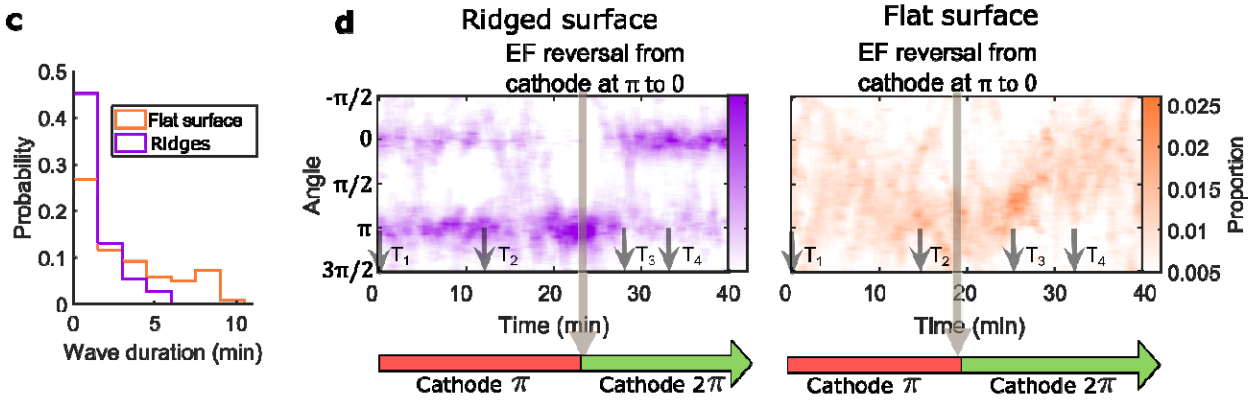

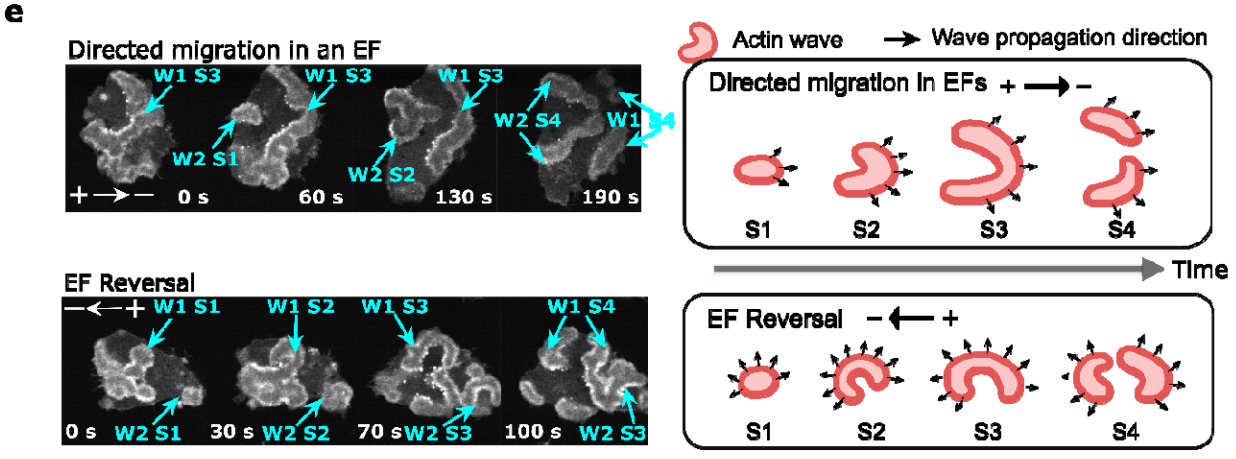

Fig. 3. EFs guide actin waves. a, b Optical-flow analysis of actin-wave dynamics in giant cells on ridged and flat surfaces. The top row shows a time series of limE images for giant cells overlaid with optical-flow vectors, the color of which is coded according to the color wheel. The accompanying polar plots show the corresponding orientation displacements of optical-flow vectors. For both a and b the EF was turned on at 0 min. The bottom time stamp indicates when the EF was reversed from the cathode being on the right (red) to the cathode being on the left (green). **c.** Distributions of wave duration from 3 independent days of experiments. The distributions were weighted by wave area, because the number of long-lasting large waves on flat surfaces (N_{wave} = 359) is smaller than the number of short-lived small patches on ridged surfaces (N_{wave} = 658). Correspondingly, the absolute waves counts do not match the pixel-based, optical-flow analysis in a and b. Based on a two-sample t-test on the wave areas on flat surfaces vs. on ridges, the null hypothesis was rejected at the 5% significance level with $p = 2 \times 10^{-15}$. **d.** Kymographs of orientation displacements of optical-flow vectors. The *x*-axes of the kymographs represent time, and the *y*-axes represent orientation. The colors represent the proportions. The EF was turned on at time T_1, and was reversed at the time denoted by the black arrow **e.** LimE snapshots showing the patterns of actin-wave expansion during steady directed migration in a constant EF (top) and after reversing the EF direction (bottom). The blue arrows point to specific stages of wave expansion. W: Wave, S: Stage of wave expansion. The right panel is a cartoon illustrating the patterns of actin-wave expansion during directed migration in EFs (top) and after EFs were reversed (bottom).

Figure 3 – source data 1. Related to Fig. 3c

Subcellular spatial inhomogeneity of the response to EFs on nanoridges.

Although waves in migrating *D. discoideum* cells localize predominantly at the leading edge (Weiner et al., 2007; Zhao et al., 2002), waves are observed across the basal layer in giant *D. discoideum* cells. We analyzed the smaller, shorter-lived waves on nanoridges. Although the wave locations were distributed essentially uniformly throughout cells in the absence of an EF, more waves were generated at the cell fronts in the presence of an EF (Fig. 4a and Video 9). In addition, the average area per wave was larger near the front of cells in an EF (Fig. 4b). We also measured the wave properties in the single cells scattered throughout the field of view but did not observe a corresponding gradient of wave properties among single cells closer to the cathode versus the cells closer to the anode. This result indicates that the spatial inhomogeneity shown in Figs. 4a, b was caused by the EF rather than by the absolute electrical potential relative to the ground (Fig. 4 – figure supplement 1).

We explored the response of this inhomogeneity to EF reversal by tracking each wave location relative to the cell centroid in the 12 min following EF reversal (Fig. 4c). New waves started to appear near the side of the cell facing the new cathode within 3 min (Fig. 4c, left region of P_2), whereas the complete inhibition of wave generation near the old cell front took longer (Fig. 4c, right region of P_5). This observation suggests that the initiation at a new cell front and the inhibition of waves at the old front are regulated by two distinct processes with different timescales.

Next, we looked at the time required to switch propagation direction in different subcellular regions following EF reversal. The basal membrane was segmented into an “old front” region

(facing the original cathode) and a “new front” region (facing the new cathode), as illustrated in Fig. 4d. The distributions of wave propagation directions show that waves in the new front region switched their preferential direction at ~4 min. In contrast, waves in the old front region changed their preferential direction on a time scale of ~ 7 min (Figs. 4 e, f). Our analysis further shows that larger waves in the old fronts are less sensitive to EF reversal than those in the new fronts (Fig. 4 – figure supplement 2).

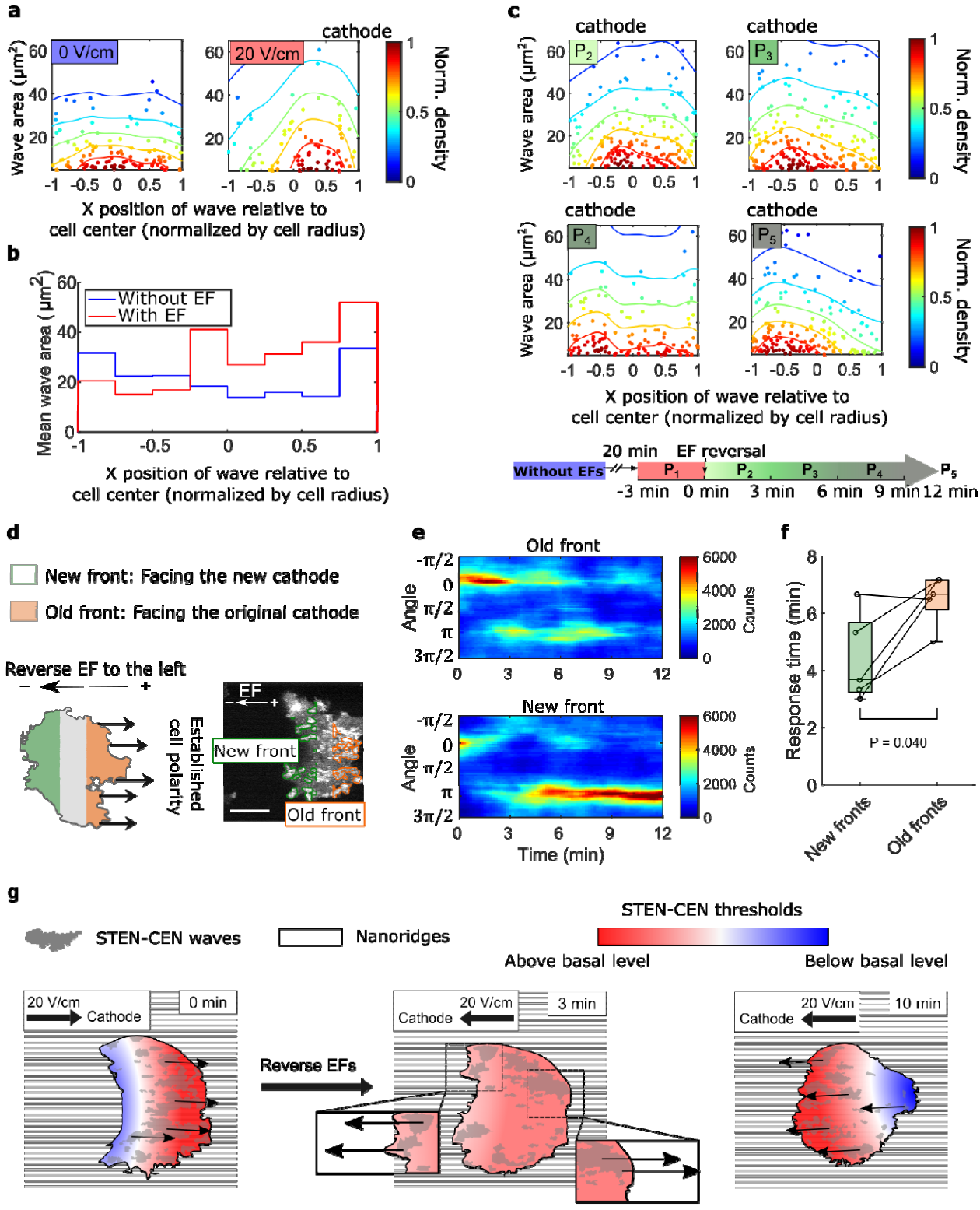

306 **Fig. 4. Spatial inhomogeneity of the response to EFs on nanoridges. a.** Density scatter plots

307 of the wave area vs. x position of the wave relative to the cell center. Nanoridges and EF are

orientated in the x-direction. The difference of x coordinates of cell center and wave location was calculated, then the value was further normalized by the cell radius. Each point represents a wave, and all the points were collected from 5 independent experiments. The left plot is for a period in which there was no EF (N_{wave} = 296), and the right plot is for a period in which there was a 20 V/cm EF, during which the cells exhibited steady directional migration (N_{wave} = 224) . For each experiment without an EF, the EF was always turned on several minutes later. Thus, we defined the direction in which cathode was located in the presence of an EF as the positive direction in the absence of an EF. The color code corresponds to the density of points. **b.** Average wave area in sub-cellular regions. The points in a were sectioned, based on their x position relative to the cell center (normalized by cell radius) at a bin size of 0.25 (8 sections in total from -1 to 1), and calculated the average wave area in each section. **c.** Changes in actin waves' spatial distribution in response to EF reversal; data from 6 independent experiments. The color of each plot is coded according to the timeline displayed at the bottom of the panel. P_2-P_5: The EF was reversed, and cells gradually developed polarization towards the new cathode. The number of waves in each plot: N_{p2} = 272, N_{p3} = 277, N_{p4} = 193, N_{p5} = 246. **d.** A schematic illustrating the old and new fronts of giant cells when the EF was reversed. **e.** Time stacks of orientation distributions of optical-flow vectors at an old front and a new front. The EF was reversed from the cathode being at the right (0) to the cathode being at the left (π) at 0 min. **f.** Comparisons of response time between new fronts (green) and old fronts (orange) from multiple experiments (N_{cell} = 5). The *P*-value was calculated using a pairwise t-test at the 5% significance level. **g.** Cartoon illustrating different time scales of local wave propagation and global rearrangement of STEN-CEN thresholds, in response to EF reversal.

Figure 4 – source data 1. Related to Fig. 4a-c

Discussion

By employing giant cells, in which the cortical waves are disentangled from cell motion, we demonstrate that EFs modulate cortical wave dynamics directly, providing a mechanism for cell guidance by EFs (Fig. 1 c, b, d). Our use of nanoridges to generate quasi-1D waves that are small, short-lived, and unable to turn (Fig. 1c) enabled detailed quantification of wave properties, demonstrating that EFs directly affect the abundance, locations, and directions of cortical waves.

EFs guide cortical wave dynamics

Previous studies have suggested that the basal cortical waves in *D. discoideum* are insensitive to external chemotactic gradients, whereas "pseudopods" at other regions in the same cells can be guided (Lange et al., 2016). This conclusion is surprising because the biochemical events traveling with the waves are the same as those occurring on pseudopods, and pseudopods with the dorsal cups on the same cells do respond to chemoattractants. Also, similar cortical waves in human mammary epithelial cells can be guided effectively by epidermal growth factors (Zhan et al., 2020). Additional input from the greater contact of giant *D. discoideum* cells with the surface may outweigh the effect of applied chemical gradients on the basal waves. Other studies have shown that single cells can integrate combinations of external chemical and mechanical stimuli.

Our work shows that in giant cells, waves of both F-actin polymerization (Fig. 3) and its upstream regulator PIP3 (Fig. 1 – figure supplement 1) are indeed guided by EFs. These biased biochemical and biomechanical events lead to more protrusions at the cell front than at the cell back, thus driving cell migration (Fig. 2 – figure supplement 2). The development of the biased

wave activities takes ~10 min following the introduction of an EF (Fig. 2a and Fig. 3), which is much slower than the timescale of surface-receptor-regulated chemotaxis. The high resistance of the cell membrane limits the effects of EFs on intracellular components, but EFs may act on the charged lipids and molecular clusters. Thus, we suspect that the slow response results from the electrophoresis of the charged membrane components involved in wave formation, which has a characteristic time scale of 5 to 10 min (Allen et al., 2013; McLaughlin & Poo, 1981).

We further explored the dynamics in response to EF reversal at the subcellular level using nanotopography (Fig 4). We observed that the new waves are induced to propagate towards the current cathode within 2 to 3 min (Fig. 4e and Fig.4 – figure supplement 2), suggesting that waves themselves can adapt quickly to the changing electrical environments. Because we only observed the fast adaptation on ridged surfaces, this phenomenon may be related to the shorter wave lifetimes on nanoridges than on flat surfaces. A short lifetime allows waves to be nucleated at a higher rate on the nanoridges, leading to a rapid directional response. During this process, the EF may regulate the wave nucleation through locally changing specific charged lipids, ion fluxes, or local pH gradients (Crevenna et al., 2013; Frantz et al., 2008; Köhler et al., 2012; Martin et al., 2011; Zhou & Pang, 2018).

EFs modulate the thresholds of the excitable wave system

Recent studies have shown that the cortical wave system can be described as a coupled signal transduction and cytoskeletal excitable network. Based on both simulation and experimental studies (Bhattacharya et al., 2020; Miao et al., 2017), it has been shown that the wave ranges,

durations, and speeds are determined by the local threshold of activation, which in turn are regulated by the relative levels of activators and inhibitors (Miao et al., 2017, 2019).

Our quantification shows that guided waves become larger, faster, and more persistent in an EF (Fig. 2), indicating that the excitable system is closer to its threshold for activation (Miao et al., 2019). This effect may arise from enhanced positive feedback, reduced negative feedback, or both. We further find that wave nucleation is enhanced at the cell front and suppressed at the back (Fig. 4a, b). This subcellular inhomogeneity is consistent with a biased excitable network framework (Iglesias & Devreotes, 2012; Meinhardt, 1999; Tang et al., 2014; Xiong et al., 2010), which was added to the STEN-CEN model to introduce an internal spatial gradient in the local threshold of wave initiation, akin to cell polarity.

Local excitation and global inhibition (Xiong et al., 2010), LEGI, schemes have effectively recreated the features of both fast directional sensing and stable polarity in response to chemical signals, which can lead to robust biased excitable network. Both directional sensing and stable polarity can lead to a robust biased excitable network. For chemical signals, the directional response from PIP3 occurs within seconds, whereas the establishment of stable polarity usually requires many minutes. However, based on our analysis, establishing both directional response (Fig. 3) and polarity (Fig. 4) in response to EFs requires 5 to 10 min. It is worth noting that PIP3 waves also sense EFs on a time scale of minutes (Fig. 1 – figure supplement 1). Our observation suggests that EFs act on the polarity establishment rather than directional sensing. This hypothesis is supported by a recent study showing that G-protein-coupled receptors (GPCRs),

398 which are the regulator in the LEGI model for *D. discoideum* that allows for sensing
399 chemoattractant on timescales of seconds, are not essential for electrotaxis (Zhao et al., 2002).
400
401 **EFs act on waves, and waves determine cell behaviors**
402 Our results raise the possibility that cortical wave dynamics are modulated directly by EFs and
403 that the waves in turn mediate cellular response. Waves travel across cell membranes to
404 coordinate the trailing edge with the front edge, and the cytoskeletal components in cortical
405 waves are involved in developing the stable polarity. On the other hand, the duration and turning
406 capacity of STEN-CEN waves directly impact the speed and characteristics of the cellular
407 response to EFs (Fig. 3) on a longer timescale than that of surface-receptor-regulated chemotaxis.
408
409 Our results shed light on how EFs modulate protrusions. Previous studies have shown that
410 various protrusions that drive cell motion, such as filopodia, lamellipodia (Miao et al., 2019), and
411 macropinocytotic cups (Video 4), are always associated with expanding waves near cell
412 perimeter. Our previous work has shown that changing wave properties by perturbing STEN-
413 CEN states leads to the transition of protrusion profiles, which indicates that wave properties
414 dictate the properties of the protrusions (Miao et al., 2019). Here we showed that EFs can alter
415 the waves differently on the two ends of the cell (Fig. 4a). As a result of these spatially
416 inhomogeneous wave properties, protrusions become more abundant and larger on one side of
417 the cell versus the other, which eventually leads to guidance of cell migration.
418
419 On flat surfaces, a slow U-turn is observed following EF reversal, whereas on nanoridges, faster
420 switching is observed. Thus, the response of migrating cells to a changing guidance cue can be

421 predicted from the characteristics of the waves driving the migration process. Indeed, the U-turn
422 behaviors of neutrophils and differentiated, single *D. discoideum* cells in response to EF reversal
423 (Hind et al., 2016; Sato et al., 2007; Srinivasan et al., 2003; Xu et al., 2003), which are usually
424 ascribed to stable cell polarity, may instead reflect the persistence and 2D turning behavior of
425 cortical waves in these environments (Fig. 3).
426
427 Nanoridges allow us to shed further light on the multiscale character of the system, because cells
428 include both short, 1D waves on the basal plane, and longer-lasting, 2D waves on the dorsal
429 plane. The different response times on the subcellular level due to different wave behaviors (Fig.
430 4 – figure supplement 2) provide strong evidence that cortical waves act as direct mediators of
431 EFs. Waves on different planes are similar in composition but are impacted differently by the EF.
432 We observed fast switching of wave directions in the basal plane near the ridged substrate and
433 slower turning of the waves in the dorsal plane within the same cell, indicating that the direction
434 of waves is controlled locally by external cues (Fig. 3 – figure supplement 1).
435
436 EFs provide a means to modulate cortical waves directly. On the other hand, biological
437 conditions that modulate wave characteristics may also speed up or suppress the cellular
438 response to directional cues. Longer-lasting waves offer persistence in the face of rapidly
439 changing gradients, whereas shorter waves yield faster adaptability to changing directional
440 signals. The durations of waves and their ability to turn together have a dominant effect on the
441 response of cells to an EF.

Key Resources Table

Reagent type (species) or resource	**Designation**	**Source or reference**	**Identifiers**	**Additional information**
Cell line *(D. discoideum)*	Aca null	https://doi.org/10.1016/S0092-8674(03)00081-3		The cell line was a gift from Carole A. Parent lab.
Cell line *(D. discoideum)*	PHcrac-GFP LimE-RFP	https://doi.org/10.1038/ncb3495		The cell line was a gift from Peter N. Devreotes lab.
software, algorithm	Optical flow analysis (run by MATLAB)	https://doi.org/10.1091/mbc.E19-11-0614		

Materials and Methods

Cell line

In the study, we used LimE-RFP aca null Dictyostelium discoideum (D.d.) and PHcrac-GFP/LimE-RFP D.d cell lines. LimE-RFP aca null was a gift from Carole A. Parent lab (https://doi.org/10.1016/S0092-8674(03)00081-3), and PHcrac-GFP-LimE-RFP was a gift from

448 Peter N. Devreotes lab (https://doi.org/10.1038/ncb3495). We have conducted the mycoplasma
449 contamination testing for both cell lines and did not detected contamination.
450
451 Cell culture
452 *Dictyostelium discoideum* cell lines were grown axenically in the HL5 medium. Aggregation
453 adenylyl cyclase null (ACA−) mutants, which do not produce cAMP and do not have chemotaxis
454 signal relay (Kriebel et al., 2003), were used in electrotaxis experiments to avoid chemotaxis.
455 The cells used also express limE-RFP as a reference for filamentous actin structures. G418 was
456 used as the selection medium during cell culture. For the experiments in Fig. 1/Fig.1 -
457 supplement figure 1, we used *Dictyostelium discoideum* co-expressing PHcrac-GFP and LimE-
458 RFP, and we used G418 as the selective medium. Note that an enhancement in LimE
459 concentration is associated with protrusions, as seen in fig. 2 -figure supplement 2, and that the
460 protrusions are biased to the side facing the cathode. Because protrusions are driven by F-actin
461 polymerization, we believe this observation rules out the possibility that LimE binding/unbinding
462 to/from F-actin itself is sensitive to EFs.
463
464 Electrofusion
465 Cells were washed twice with 17 mM Sorensen buffer (15 mM KH_2PO_4 and 2 mM Na_2HPO_4,
466 pH 6.0) and rolled for 30 min at a concentration of 1.5×10^7 mL^{-1}. Electrofusion was conducted
467 with a Gene Pulser Gen1 system. Three pulses of 1 kV at a 1 s interval were applied. After
468 electroporation, cells were relaxed for 5 min. Then cells were diluted to 5×10^5 mL^{-1} with normal
469 developing buffer (5 mM KH_2PO_4, 5 mM Na_2HPO_4, 2 mM $MgCl_2$ and 0.2 mM $CaCl_2$, PH 6.5)
470 and seeded into a customized electrotactic chamber, with dimensions 20 mm × 5 mm × 0.25 mm.

The aca null cell line that we used did not generate many waves in the vegetative stage, and electro-fusion with 1 kV pulses stressed the cells. Thus cells were starved for 2 h before experiments to generate more actin waves.

Nanotopography fabrication

The nanotopographic pattern used in these cell studies was fabricated through a technique known as multiphoton absorption polymerization (MAP), as described elsewhere (C. M. LaFratta et al., 2006; C. N. LaFratta et al., 2004). An ultrafast, pulsed laser beam (Coherent Mira 900-F, 76 MHz) was passed through a high-numerical-aperture microscope objective onto a photopolymerizable resin, sandwiched between glass coverslips. A LabVIEW (National Instruments) program allowed for control of the stage position and the shutter state, determining where polymerization occurred (and did not) in the resin and allowing patterning. Once fabrication was completed, the patterned sample was developed in ethanol twice for 3 min each to remove unreacted monomer. The polymerized structure was baked at 110 °C for at least 1 h.

To produce the necessary number of replicate patterns with the same dimensions, an adapted version of replica molding was performed (Sun et al., 2018). A hard polydimethylsiloxane (*h*-PDMS) film containing hexanes to increase the resolution of feature replication was spin-coated onto the functionalized structure made from MAP. The film was allowed to sit on the structure for 2 h at room temperature and was then baked at 60 °C for 1 h. Regular PDMS (Sylgard 184) was prepared at a 10:1 ratio of elastomer base to the curing agent by degassing and mixing. The PDMS was poured onto the *h*-PDMS film, and molding was completed by baking at 60 °C for an

493 additional 70 min. The final mold was peeled from the glass slide supporting the MAP-patterned
494 structure.
495
496 The mold was used to produce replicas of the original pattern. A drop of the same acrylic resin
497 was placed on the patterned area of the PDMS mold, and then an acrylate-functionalized glass
498 coverslip was pressed firmly on top, spreading the sandwiched drop. Tape secured this system in
499 place. The resin was cured for a total of 5 min under a UV lamp (Blak-ray), producing a polymer
500 film. It should be noted that the PDMS mold is the negative relief pattern of the structure made
501 using MAP. Therefore, samples (or replicas) of the original pattern could be produced on a
502 relatively large scale with this method. The replicas were soaked in ethanol for at least 12 h
503 before use in the cell studies. We fabricated flat surface samples by using a PDMS mold with a
504 smooth surface.
505
506 Lattice light-sheet microscopy
507 The 3i lattice light-sheet microscope in the Johns Hopkins School of Medicine Microscope
508 Facility was used for 2-color, 3D imaging. Vegetative, single *Dictyostelium* cells were seeded on
509 a circular 5 mm coverslip patterned with nanoridges, which was immersed in a bath of standard
510 developing buffer throughout imaging.
511
512 Electrotaxis experiments
513 We 3D-printed electrotaxis chambers (Fig. 2 – figure supplement 1) with dimensions of 20 mm ×
514 5 mm × 0.25 mm and composed of a clear resin using a Formlabs Form2 3D-printer. Agar
515 bridges were used to isolate cell media from electrodes to minimize electrochemical products

and pH changes. 20 V/cm constant EFs were applied. Time-lapse images of the phase-contrast channel and the RFP/GFP channel were recorded using PerkinElmer spinning-disk microscope at a frame rate of 0.1 frames/s (Yokogawa CSU-X1 spinning-disk scan head (5000 rpm)) with Hamamatsu EMCCD camera and Volocity analysis software.

Optical-flow analysis and model fitting of actin polymerization dynamics

We applied the Lukas-Kanade optical-flow method to quantify the direction of the intensity flow in fluorescence videos. This algorithm produced pixel-basis vector fields of intensity motion. Before applying the optical-flow algorithm, each image was smoothed by a 2D Gaussian filter (σ = 3) to reduce noise. After the smoothing, we further removed the flow vectors created by noise using optical-flow reliability as our criterion. The reliability is defined as the smallest eigenvalues of the $A^T wA$ matrix, where w is a Gaussian weight matrix and A is the intensity gradient matrix. The size of the weight matrix for *D. discoideum* was set at 19 × 19, with standard deviation σ = 2 (0.42 μm).

We built a bimodal von Mises model to compare the actin and cellular responses accurately. A von Mises distribution is given by

$$f_{VM}(\theta|\mu,\kappa) = \frac{e^{\kappa\cos(\theta-\mu)}}{2\pi I_0(\kappa)} \quad . \tag{2}$$

where the peak location is μ and the concentration κ. The orientation distribution of optical-flow vectors at each time point is fit with two von Mises distributions

$$f(\theta|\mu_1,\mu_2,\kappa,p_1,p_2) = p_1 f_{VM}(\theta|\mu_1,\kappa) + p_2 f_{VM}(\theta|\mu_1+\pi,\kappa) \tag{3}$$

where p is the proportion of each component. We use the constraints

$$\mu_1 - \mu_2 = \pi \tag{4}$$

539 and

540 $$p_1 + p_2 = 1\ . \quad (5)$$

541 Maximum likelihood estimation (MLE) is applied to estimate model parameters based on the
542 orientation of all the optical-flow vectors every 12 frames (2 min). With this model, we can
543 quantitatively study the temporal change of actin dynamics. The preferential direction is defined
544 as the μ with the largest proportion p at each time point.

545

546 Quantification of actin wave properties

547 The segmentation of actin waves was conducted based on the combined information from
548 fluorescence intensities and optical flow. We first applied the kmeans (k = 3) cluster (Kanungo et
549 al., 2002) to pick up the bright regions in the limE-RFP videos, then only kept the moving
550 objects by applying the reliability mask from the optical-flow analysis.
551 To classify the large actin structures composed of substructures moving independently, we
552 considered the optical flow at the edges of the large structure (Fig. 2c). If the optical-flow vectors
553 were moving in the same direction at both edges, the large structure was classified as a single
554 wave. Otherwise, the large structure was divided into multiple smaller patches. In the latter case,
555 a pronounced boundary was detectable between two substructures, then we used the detected
556 boundary to divide the large structure into multiple substructures.

557

558 After classification, we measured properties such as wave speed, wave duration, and wave area
559 to characterize STEN-CEN. Wave speed was measured by tracking the clusters of optical-flow
560 vectors oriented in similar directions. The detailed algorithm can be found in a prior publication
561 (Lee et al., 2020). To measure wave duration, we first tracked actin waves using a customized,

562 multi-object tracking tool based on the overlapping areas between frames. A unique
563 identification number was assigned to each wave, then wave duration, wave area (measured by
564 the Matlab function regionprops) were recorded for each wave.
565

566 **Acknowledgments:** We thank Q. Qing and M. Zhao for the discussion. **Competing interests:**
567 The authors declare that they have no competing interests.
568

569 **References:**

570 Allen, G. M., Mogilner, A., & Theriot, J. A. (2013). Electrophoresis of cellular membrane
571 components creates the directional cue guiding keratocyte galvanotaxis. *Current Biology*,
572 *23*(7), 560–568. https://doi.org/10.1016/j.cub.2013.02.047
573 Bhattacharya, S., Banerjee, T., Miao, Y., Zhan, H., Devreotes, P. N., & Iglesias, P. A. (2020).
574 Traveling and standing waves mediate pattern formation in cellular protrusions. *Science*
575 *Advances*, *6*(32), eaay7682. https://doi.org/10.1126/sciadv.aay7682
576 Bhattacharya, S., & Iglesias, P. A. (2018). Controlling excitable wave behaviors through the
577 tuning of three parameters. *Biological Cybernetics*, *113*(1), 61–70.
578 https://doi.org/10.1007/s00422-018-0771-0
579 Bhattacharya, S., Miao, Y., Devreotes, P. N., & Iglesias, P. A. (2019). A Coupled Excitable
580 Network Model Dictates Cortical Wave Patterns and Controls Cellular Protrusion
581 Morphology. *Biophysical Journal*, *116*(3), 121a. https://doi.org/10.1016/j.bpj.2018.11.675
582 Bretschneider, T., Anderson, K., Ecke, M., Müller-Taubenberger, A., Schroth-Diez, B.,
583 Ishikawa-Ankerhold, H. C., & Gerisch, G. (2009). The three-dimensional dynamics of actin
584 waves, a model of cytoskeletal self-organization. *Biophysical Journal*, *96*(7), 2888–2900.

https://doi.org/10.1016/j.bpj.2008.12.3942

Cortese, B., Palamà, I. E., D'Amone, S., & Gigli, G. (2014). Influence of electrotaxis on cell behaviour. *Integrative Biology (United Kingdom)*, *6*(9), 817–830. https://doi.org/10.1039/c4ib00142g

Crevenna, A. H., Naredi-Rainer, N., Schonichen, A., Dzubiella, J., Barber, D. L., Lamb, D. C., & Wedlich-Söldner, R. (2013). Electrostatics control actin filament nucleation and elongation kinetics. *Journal of Biological Chemistry*, *288*(17), 12102–12113. https://doi.org/10.1074/jbc.M113.456327

Devreotes, P. N., Bhattacharya, S., Edwards, M., Iglesias, P. A., Lampert, T., & Miao, Y. (2017). Excitable Signal Transduction Networks in Directed Cell Migration. *Annual Review of Cell and Developmental Biology*, *33*(1), annurev-cellbio-100616-060739. https://doi.org/10.1146/annurev-cellbio-100616-060739

Driscoll, M. K., Sun, X., Guven, C., Fourkas, J. T., & Losert, W. (2014). Cellular contact guidance through dynamic sensing of nanotopography. *ACS Nano*, *8*(4), 3546–3555. https://doi.org/10.1021/nn406637c

Ermentrout, G. B., Hastings, S. P., & Troy, W. C. (1984). Large Amplitude Stationary Waves in an Excitable Lateral-Inhibitory Medium. *SIAM Journal on Applied Mathematics*, *44*(6), 1133–1149. https://doi.org/10.1137/0144081

Flemming, S., Font, F., Alonso, S., & Beta, C. (2020). How cortical waves drive fission of motile cells. *Proceedings of the National Academy of Sciences of the United States of America*, *117*(12), 6330–6338. https://doi.org/10.1073/pnas.1912428117

Frantz, C., Barreiro, G., Dominguez, L., Chen, X., Eddy, R., Condeelis, J., Kelly, M. J. S., Jacobson, M. P., & Barber, D. L. (2008). Cofilin is a pH sensor for actin free barbed end

formation: role of phosphoinositide binding. *Journal of Cell Biology*, *183*(5), 865–879. https://doi.org/10.1083/jcb.200804161

Gerhardt, M., Ecke, M., Walz, M., Stengl, A., Beta, C., & Gerisch, G. (2014). Actin and PIP3 waves in giant cells reveal the inherent length scale of an excited state. *Journal of Cell Science*, *127*(20), 4507–4517. https://doi.org/10.1242/jcs.156000

Gerisch, G. (2010). Self-organizing actin waves that simulate phagocytic cup structures. *PMC Biophysics*, *3*(1), 1–9. https://doi.org/10.1186/1757-5036-3-7

Harvath, L., Robbins, D., Russell, A. A., & Seamon, K. B. (1991). Elevation of cAMP differentially affects chemotactic responsiveness . *The Journal of Immunology*, *146 (1) 22*(Vol. 146, Issue 1).

Hind, L. E., Vincent, W. J. B., & Huttenlocher, A. (2016). Leading from the Back: The Role of the Uropod in Neutrophil Polarization and Migration. *Developmental Cell*, *38*(2), 161–169. https://doi.org/10.1016/j.devcel.2016.06.031

Iglesias, P. A., & Devreotes, P. N. (2012). Biased excitable networks: How cells direct motion in response to gradients. *Current Opinion in Cell Biology*, *24*(2), 245–253. https://doi.org/10.1016/j.ceb.2011.11.009

Kanungo, T., Mount, D. M., Netanyahu, N. S., Piatko, C. D., Silverman, R., & Wu, A. Y. (2002). An efficient k-means clustering algorithms: Analysis and implementation. *IEEE Transactions on Pattern Analysis and Machine Intelligence*, *24*(7), 881–892. https://doi.org/10.1109/TPAMI.2002.1017616

Ketchum, C. M., Sun, X., Suberi, A., Fourkas, J. T., Song, W., & Upadhyaya, A. (2018). Subcellular topography modulates actin dynamics and signaling in B-cells. *Molecular Biology of the Cell*, *29*(14), 1732–1742. https://doi.org/10.1091/mbc.E17-06-0422

631 Köhler, S., Schmoller, K. M., Crevenna, A. H., & Bausch, A. R. (2012). Regulating Contractility
632 of the Actomyosin Cytoskeleton by pH. *Cell Reports*, *2*(3), 433–439.
633 https://doi.org/10.1016/j.celrep.2012.08.014
634 Kriebel, P. W., Barr, V. A., & Parent, C. A. (2003). Adenylyl cyclase localization regulates
635 streaming during chemotaxis. *Cell*, *112*(4), 549–560. https://doi.org/10.1016/S0092-
636 8674(03)00081-3
637 LaFratta, C. M., Li, L., & Fourkas, J. T. (2006). Soft-lithographic replication of 3D
638 microstructures with closed loops. *Proceedings of the National Academy of Sciences of the*
639 *United States of America*, *103*(23), 8589–8594. https://doi.org/10.1073/pnas.0603247103
640 LaFratta, C. N., Baldacchini, T., Farrer, R. A., Fourkas, J. T., Teich, M. C., Saleh, B. E. A., &
641 Naughton, M. J. (2004). Replication of two-photon-polymerized structures with extremely
642 high aspect ratios and large overhangs. *Journal of Physical Chemistry B*, *108*(31), 11256–
643 11258. https://doi.org/10.1021/jp048525r
644 Lange, M., Prassler, J., Ecke, M., Müller-Taubenberger, A., & Gerisch, G. (2016). Local Ras
645 activation, PTEN pattern, and global actin flow in the chemotactic responses of oversized
646 cells. *Journal of Cell Science*, *129*(18), 3462–3472. https://doi.org/10.1242/jcs.191148
647 Lee, R. M., Campanello, L., Hourwitz, M. J., Alvarez, P., Omidvar, A., Fourkas, J. T., & Losert,
648 W. (2020). Quantifying topography-guided actin dynamics across scales using optical flow.
649 *Molecular Biology of the Cell*, *31*(16), 1753–1764. https://doi.org/10.1091/mbc.e19-11-
650 0614
651 Lin, F., Baldessari, F., Gyenge, C. C., Sato, T., Chambers, R. D., Santiago, J. G., & Butcher, E.
652 C. (2008). Lymphocyte Electrotaxis In Vitro and In Vivo. *The Journal of Immunology*,
653 *181*(4), 2465–2471. https://doi.org/10.4049/jimmunol.181.4.2465

654 Martin, C., Pedersen, S. F., Schwab, A., & Stock, C. (2011). Intracellular pH gradients in
655 migrating cells. *American Journal of Physiology - Cell Physiology*, *300*(3), 490–495.
656 https://doi.org/10.1152/ajpcell.00280.2010
657 McLaughlin, S., & Poo, M. M. (1981). The role of electro-osmosis in the electric-field-induced
658 movement of charged macromolecules on the surfaces of cells. *Biophysical Journal*, *34*(1),
659 85–93. https://doi.org/10.1016/S0006-3495(81)84838-2
660 Meinhardt, H. (1999). Orientation of chemotactic cells and growth cones: Models and
661 mechanisms. *Journal of Cell Science*, *112*(17), 2867–2874.
662 https://doi.org/https://doi.org/10.1242/jcs.112.17.2867
663 Miao, Y., Bhattacharya, S., Banerjee, T., Abubaker□Sharif, B., Long, Y., Inoue, T., Iglesias, P.
664 A., & Devreotes, P. N. (2019). Wave patterns organize cellular protrusions and control
665 cortical dynamics. *Molecular Systems Biology*, *15*(3), 1–20.
666 https://doi.org/10.15252/msb.20188585
667 Miao, Y., Bhattacharya, S., Edwards, M., Cai, H., Inoue, T., Iglesias, P. A., & Devreotes, P. N.
668 (2017). Altering the threshold of an excitable signal transduction network changes cell
669 migratory modes. *Nature Cell Biology*, *19*(4), 329–340. https://doi.org/10.1038/ncb3495
670 Neumann, E., Gerisch, G., & Opatz, K. (1980). Cell fusion induced by high electric impulses
671 applied to Dictyostelium. *Naturwissenschaften*, *67*(8), 414–415.
672 https://doi.org/10.1007/BF00405493
673 Sato, M. J., Kuwayama, H., Van Egmond, W. N., Takayama, A. L. K., Takagi, H., Van Haastert,
674 P. J. M., Yanagida, T., & Ueda, M. (2009). Switching direction in electric-signal-induced
675 cell migration by cyclic guanosine monophosphate and phosphatidylinositol signaling.
676 *Proceedings of the National Academy of Sciences of the United States of America*, *106*(16),

677 6667–6672. https://doi.org/10.1073/pnas.0809974106

678 Sato, M. J., Ueda, M., Takagi, H., Watanabe, T. M., Yanagida, T., & Ueda, M. (2007). Input-
679 output relationship in galvanotactic response of Dictyostelium cells. *BioSystems*, *88*(3),
680 261–272. https://doi.org/10.1016/j.biosystems.2006.06.008

681 Srinivasan, S., Wang, F., Glavas, S., Ott, A., Hofmann, F., Aktories, K., Kalman, D., & Bourne,
682 H. R. (2003). Rac and Cdc42 play distinct roles in regulating PI(3,4,5)P3 and polarity
683 during neutrophil chemotaxis. *Journal of Cell Biology*, *160*(3), 375–385.
684 https://doi.org/10.1083/jcb.200208179

685 Sun, X., Hourwitz, M. J., Baker, E. M., Schmidt, B. U. S., Losert, W., & Fourkas, J. T. (2018).
686 Replication of biocompatible, nanotopographic surfaces. *Scientific Reports*, *8*(1), 1–9.
687 https://doi.org/10.1038/s41598-017-19008-z

688 Tang, M., Wang, M., Shi, C., Iglesias, P. A., Devreotes, P. N., & Huang, C. H. (2014).
689 Evolutionarily conserved coupling of adaptive and excitable networks mediates eukaryotic
690 chemotaxis. *Nature Communications*, *5*, 1–13. https://doi.org/10.1038/ncomms6175

691 Veltman, D. M., Williams, T. D., Bloomfield, G., Chen, B. C., Betzig, E., Insall, R. H., & Kay, R.
692 R. (2016). A plasma membrane template for macropinocytic cups. *ELife*,
693 *5*(DECEMBER2016), 24. https://doi.org/10.7554/eLife.20085

694 Wang, M. J., Artemenko, Y., Cai, W. J., Iglesias, P. A., & Devreotes, P. N. (2014). The
695 directional response of chemotactic cells depends on a balance between cytoskeletal
696 architecture and the external gradient. *Cell Reports*, *9*(3), 1110–1121.
697 https://doi.org/10.1016/j.celrep.2014.09.047

698 Weiner, O. D., Marganski, W. A., Wu, L. F., Altschuler, S. J., & Kirschner, M. W. (2007). An
699 actin-based wave generator organizes cell motility. *PLoS Biology*, *5*(9), 2053–2063.

https://doi.org/10.1371/journal.pbio.0050221

Xiong, Y., Huang, C. H., Iglesias, P. A., & Devreotes, P. N. (2010). Cells navigate with a local-excitation, global-inhibition-biased excitable network. *Proceedings of the National Academy of Sciences of the United States of America*, *107*(40), 17079–17086. https://doi.org/10.1073/pnas.1011271107

Xu, J., Wang, F., Van Keymeulen, A., Herzmark, P., Straight, A., Kelly, K., Takuwa, Y., Sugimoto, N., Mitchison, T., & Bourne, H. R. (2003). Divergent signals and cytoskeletal assemblies regulate self-organizing polarity in neutrophils. *Cell*, *114*(2), 201–214. https://doi.org/10.1016/S0092-8674(03)00555-5

Zhan, H., Bhattacharya, S., Cai, H., Iglesias, P. A., Huang, C. H., & Devreotes, P. N. (2020). An Excitable Ras/PI3K/ERK Signaling Network Controls Migration and Oncogenic Transformation in Epithelial Cells. *Developmental Cell*, *54*(5), 608-623.e5. https://doi.org/10.1016/j.devcel.2020.08.001

Zhao, M., Jin, T., McCaig, C. D., Forrester, J. V, & Devreotes, P. N. (2002). Genetic analysis of the role of G protein-coupled receptor signaling in electrotaxis. *The Journal of Cell Biology*, *157*(6), 921–927. https://doi.org/10.1083/jcb.200112070

Zhao, M., Song, B., Pu, J., Wada, T., Reid, B., Tai, G., Wang, F., Guo, A., Walczysko, P., Gu, Y., Sasaki, T., Suzuki, A., Forrester, J. V., Bourne, H. R., Devreotes, P. N., McCaig, C. D., & Penninger, J. M. (2006). Electrical signals control wound healing through phosphatidylinositol-3-OH kinase-γ and PTEN. *Nature*, *442*(7101), 457–460. https://doi.org/10.1038/nature04925

Zhou, H. X., & Pang, X. (2018). Electrostatic Interactions in Protein Structure, Folding, Binding, and Condensation. *Chemical Reviews*, *118*(4), 1691–1741.

723 https://doi.org/10.1021/acs.chemrev.7b00305

724

Funding

Air Force Office of Scientific Research grant (FA9550-16-1-0052)

- Qixin Yang
- Yuchuan Miao
- Leonard J. Campanello
- Matt J. Hourwitz
- Bedri Abubaker-Sharif
- Abby L. Bull
- Peter N. Devreotes
- John T. Fourkas
- Wolfgang Losert

National Insititute of Health (T32 GM136577)

- Bedri Abubaker-Sharif

The funders had no role in study design, data collection, and interpretation, or the decision to submit the work for publication.

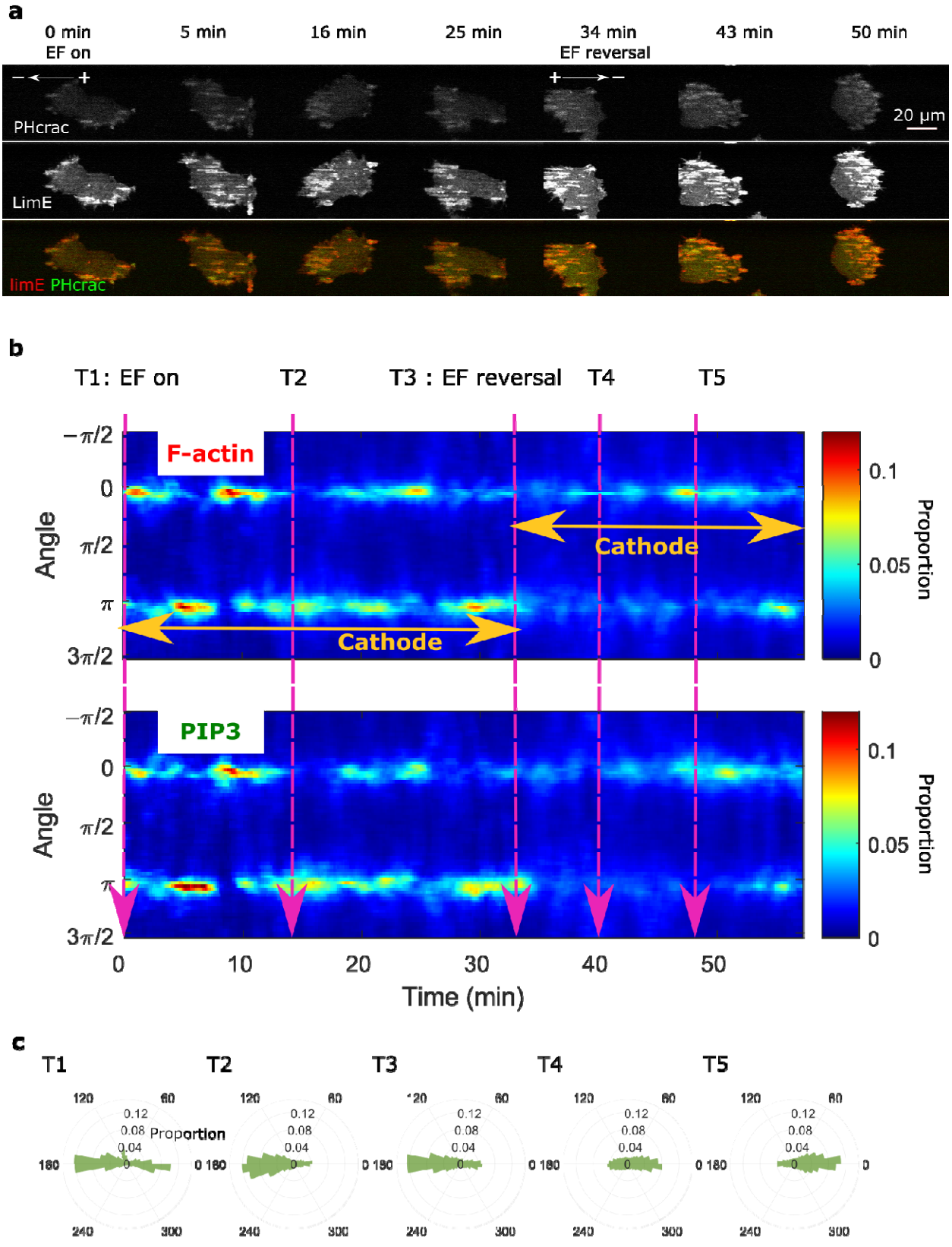

Fig. 1 – figure supplement 1. Colocalization of PIP3 and F-actin in an EF. a. Images of

744 PHcrac (top row) and LimE (middle row) in a 20 V/cm EF with the cathode located on the left.
745 The EF was turned on at 0 min and reversed at 34 min. From the combined images (bottom row),
746 it is clear that F-actin and PIP3 remained coordinated during electrotaxis. **b**. Kymograph of
747 angular distribution of F-actin (top) / PIP3 (bottom) wave motion. Optical-flow analysis was
748 applied to both the F-actin and PIP3 videos to measure wave motion. Then we stacked up the
749 angular distribution at each time point along the *x*-axis. The dynamics of F-actin/PIP3 in
750 response to EFs are similar. The color was coded according to the proportion of each bin in the
751 angular distribution. **c.** Polar plots of angular distributions from the time points specified in b.
752
753
754
755
756
757
758
759
760
761
762
763

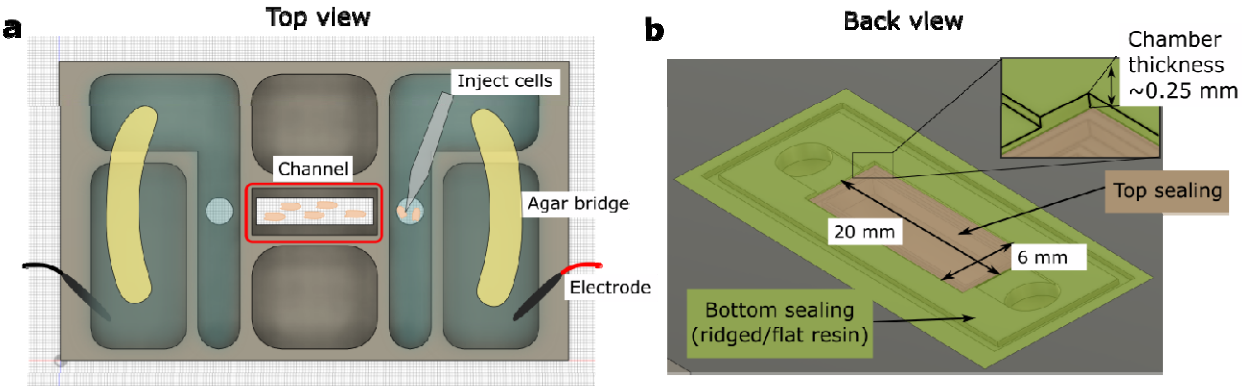

764

765 **Fig. 2 – figure supplement 1. Schematic of the 3D-printed chamber used for electrotaxis**

766 **experiments. a.** Top view of the experimental setup. **b.** Back view of the setup. Agar bridges

767 isolate the cell media from electrodes to avoid changes in pH and the generation of

768 electrochemical products. The cells were injected using pipettes into the center channel (red box

769 highlighted in a). The height of the electrotaxis channel is ~0.25 mm. The channel was sealed

770 with a large substrate coverslip and a smaller top coverslip.

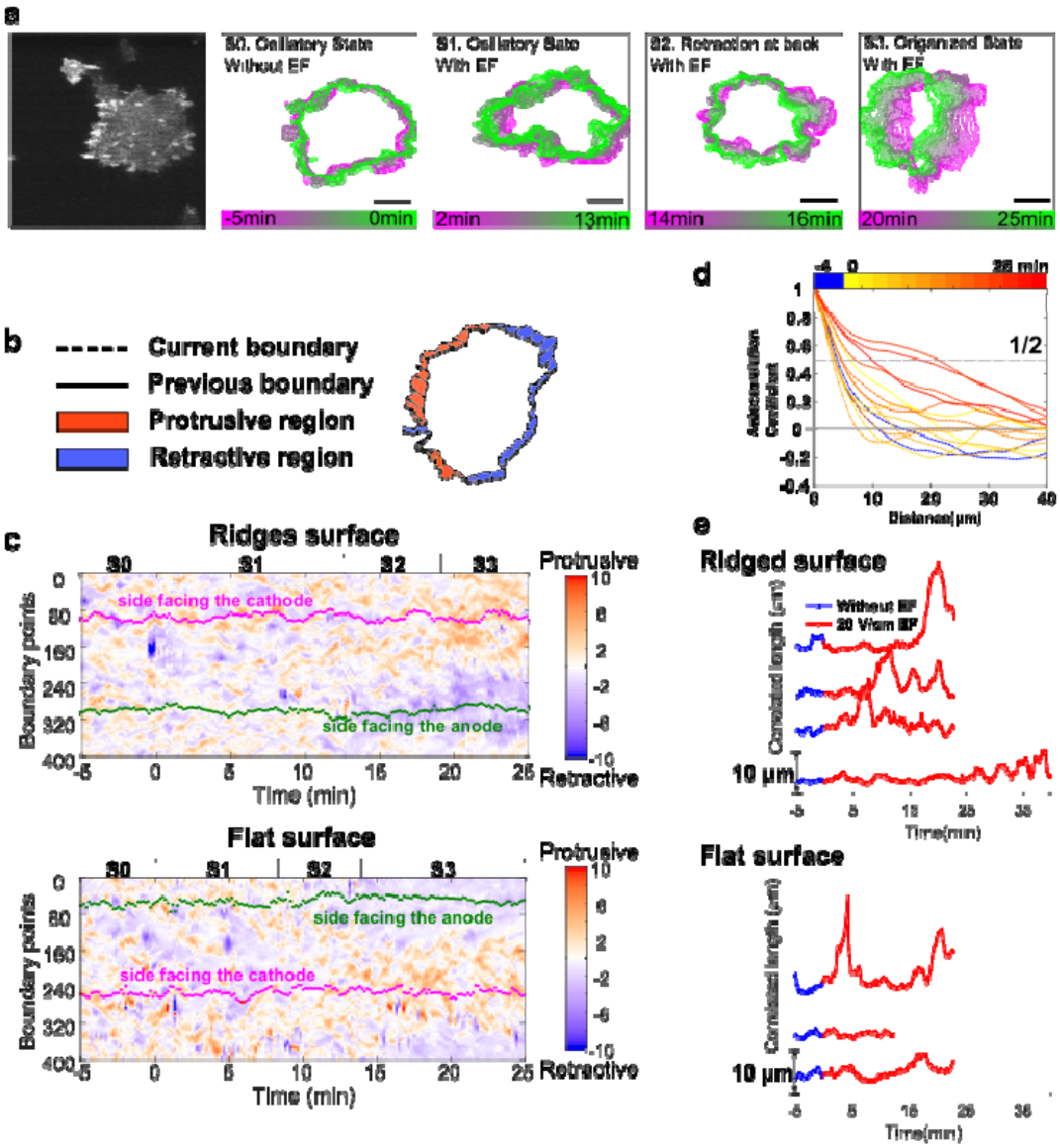

771 Fig. 2 – figure supplement 2. EFs induce keratocyte-mode migration, producing larger
772 protrusions at cell fronts. **a**. Shape dynamics of a giant *D. discoideum* cell at 10 s intervals. Cell
773 boundaries were outlined using an active contour algorithm. Boundaries are color-coded
774 according to time. Four stages were categorized: (S0) Random motion in the absence of an EF.
775 (S1) Random motion in the first 15 min in the presence of an EF. (S2) Transition state usually
776 with a retraction at the back. (S3) Steady migration state in the presence of an EF. **b**. A
777 schematic of local protrusion and retraction, where the solid line is the current frame, and the
778 dotted line represents the cell boundary 1 min later. A protrusive region (yellow) is defined as

779 one occupied in the new frame, not in the previous frame, and a retractive region (blue) is
780 defined as one occupied in the previous frame, not in the new frame. **c**. Kymograph of local
781 boundary motion. The *x*-axis represents time, the *y*-axis indicates boundary points, and the color
782 of each pixel corresponds to the speed. **d**. Correlation curves of boundary motion at different
783 time points. **e**. Correlation length (defined as the point at which curves in d reach a value of 1/2)
784 vs. time. Each curve represents an independent experiment conducted on a different day.

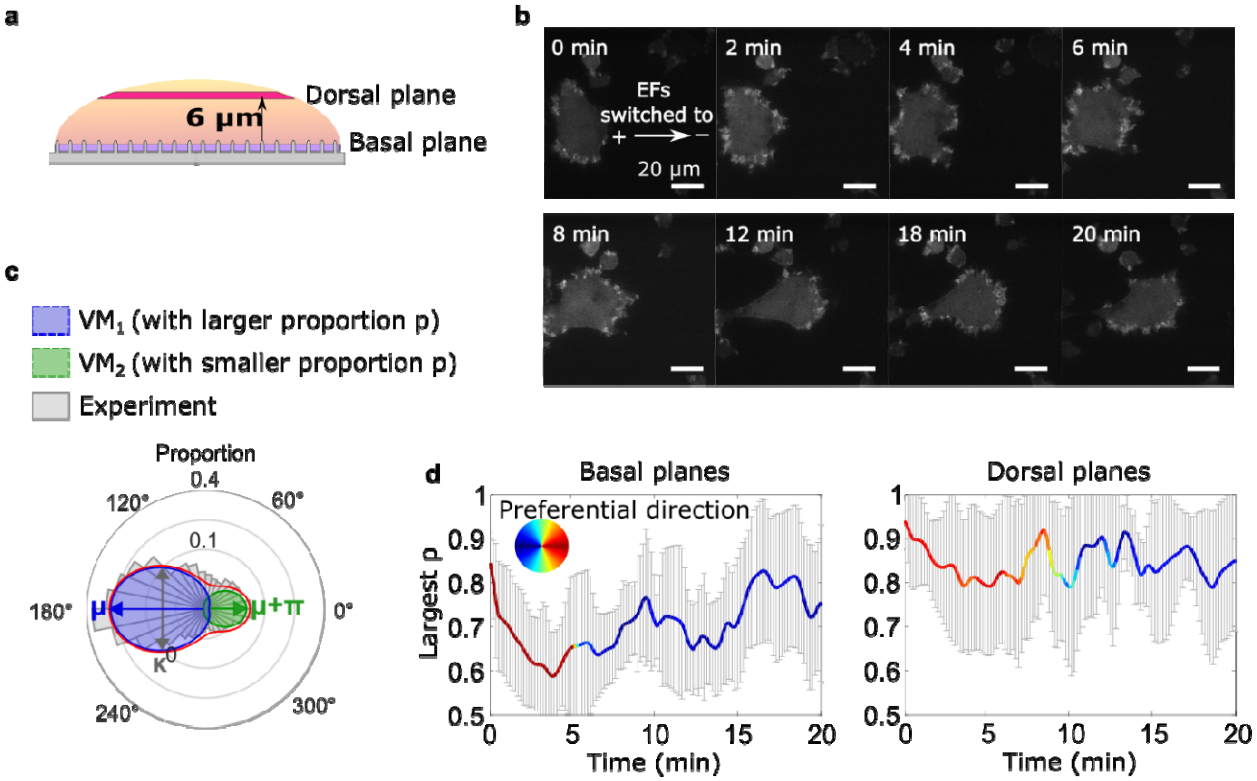

785 **Fig. 3 – figure supplement 1. Basal actin waves reverse direction on nanoridges, whereas**
786 **dorsal waves turn. a.** A schematic showing the two imaging planes used, with the morphology
787 of the substrate. **b.** LimE-RFP images recorded at the dorsal plane. Unlike the basal focal plane
788 images, which capture the complete basal wave dynamics, the dorsal plane images do not capture
789 the full dorsal wave motion. To avoid photobleaching and laser damage, we only imaged the
790 cross-section of the dorsal waves and tracked the cross-sections using optical-flow analysis.
791 **c.** A schematic introducing 4-parameter, bimodal von Mises (vM) fitting. The orientation
792 distribution (gray) was fitted to a bimodal vM distribution at each time point. The two vM
793 distributions were set to share the degree of concentration κ ($\kappa_1 = \kappa_2$), peak locations μ that were
794 set to be apart ($\mu_1 = \mu_2 + 180°$). **d.** Temporal evolution of fitting parameters in response to
795 EF reversal. Among two fitted vM distributions, the one with a larger proportion (vM_p) was
796 tracked. For both plots, the curves represent the mean p of vM_p with standard derivations from
797 multiple experiments ( ), and the colors represent the μ of vM_p.

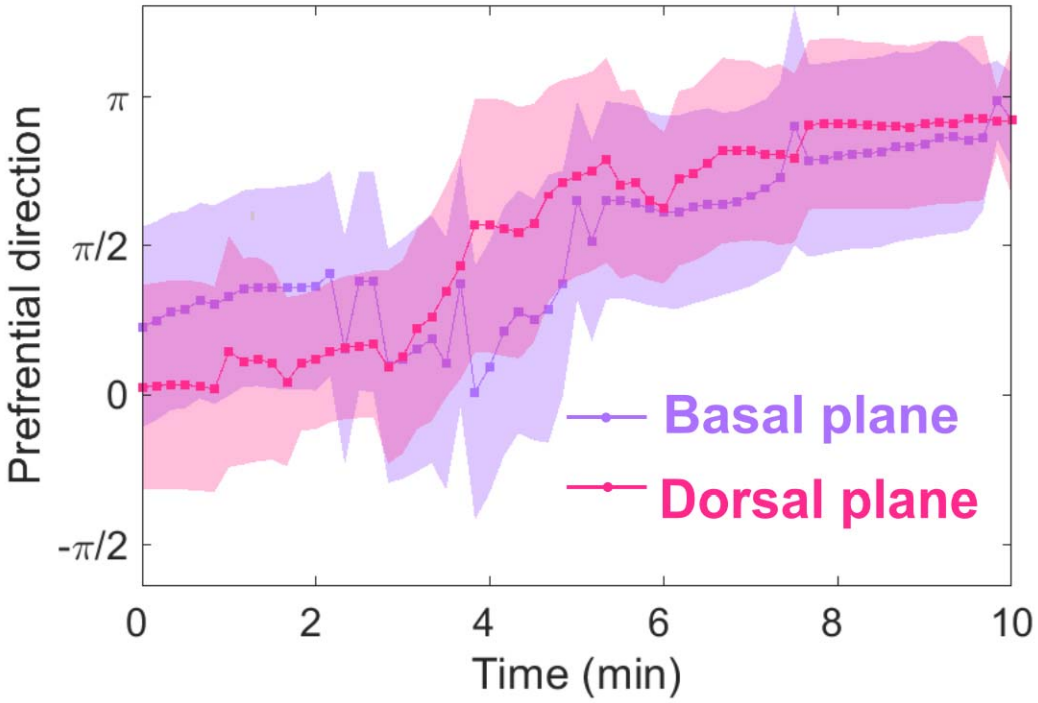

Fig. 3 – figure supplement 2. Basal and dorsal waves on flat surfaces both turn in response to EF reversal. Temporal evolution of cosine function of the fitted preferential direction of actin wave propagation for giant cells on flat surfaces. The analysis was based on $N = 3$ experiments.

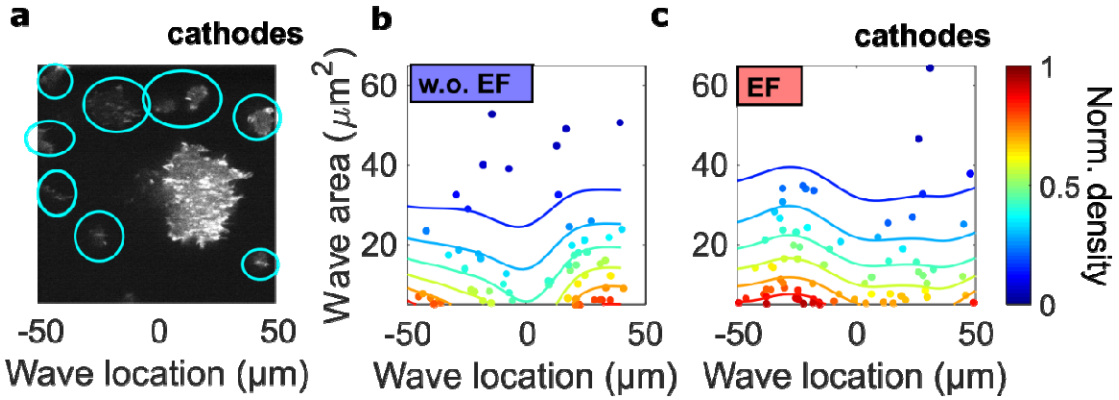

801

Fig. 4 – figure supplement 1. The spatial inhomogeneity of wave properties could be caused either by the **EF or by the external electrical potential gradient relative to the ground.** To explore these scenarios, we quantified the waves in single cells surrounding the giant cell in the field of view, where the center of the field was defined as the origin. In contrast to the giant cells, these single cells are scattered throughout the field of view but are not large enough for the potential gradient to create significant intracellular polarization. Thus, if the spatial inhomogeneity is caused by the external electrical potential gradient, we would observe a gradient of wave properties from single cells located in the region between -50 μm and 50 μm. **a.** A limE image. Single cells are highlighted with blue circles. **b, c.** Density scatter plots of wave location vs. wave area for single cells (highlighted by blue circles in a) in the absence (b) and the presence (c) of EF. Unlike in giant cells (Fig. 4a, 4b), the wave areas in single cells are spatially homogeneous. The ratio of mean wave areas in the regions nearer the cathode (location > 0) to those in regions farther from the cathodes (location < 0) was calculated for both single cells and giant cells. In giant cells, this ratio increases from 0.85 to 2.00 with an EF (Fig. 4a), whereas for single cells, the ratio is almost unchanged (1.08 without an EF and 0.98 with an EF). This analysis was based on the experiments from 4 different days.

Figure 4 – figure supplement 1- source data 1. Related to Fig. 4 – figure supplement 1.

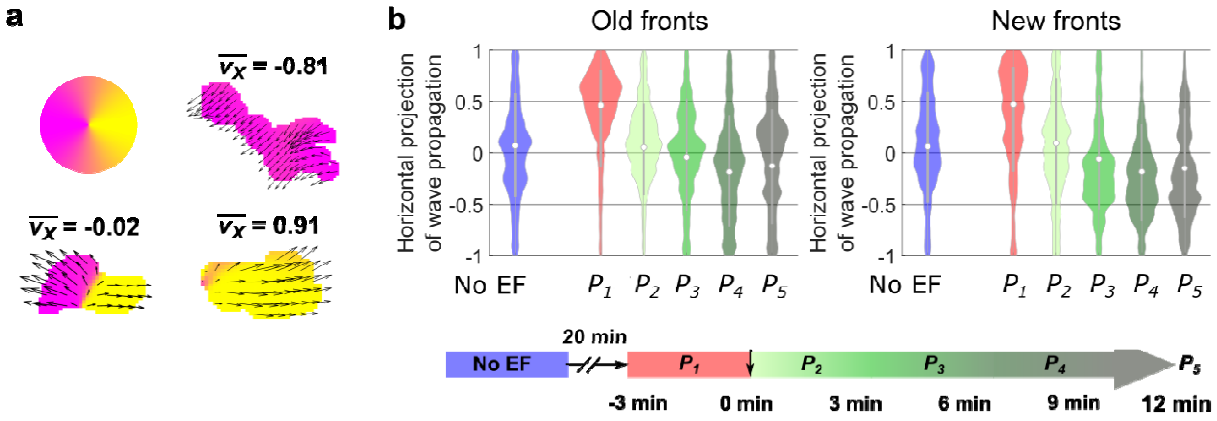

Fig. 4 – figure supplement 2. Analysis of the propagation of individual waves. a. Illustration of analysis of the propagation of individual waves. We first segmented each wave. For all of the optical-flow vectors within the wave region, we normalized the magnitudes and then calculated the *x* projection of their resultant vector (——— where is the orientation of optical-flow vector . For waves propagating unidirectionally, is close to ±1, whereas for waves extending bidirectionally, is close to 0. **b.** Violin plots of of waves near old and new fronts, at different time windows illustrated by the bottom timeline. The violin plots show the distribution of weighted by wave area, and the centered boxplot (gray bars) show the without any weighting. The analysis was based on $N = 7$ experiments performed over 4 different days. As the plots show, individual waves in the old fronts reversed their directions towards new cathodes (both violin plot and boxplot shift their centers towards <0 region) after 9 min ( ). While for waves in the new fronts, larger waves shifted their directions to new cathode within 6 min (violin plot shifts to < 0 at), and smaller wave response time is comparable to waves in the old fronts (boxplot shifts to < 0 at).

Figure 4 – figure supplement 2- source data 1. Related to Fig. 4 – figure supplement 2b.